

Article

Ni single atom catalysts for CO₂ activation

Marie-Mathilde Millet, Gerardo Algara-Siller, Sabine Wrabetz, Aliaksei Mazheika, Frank Girgsdies, Detre Teschner, Friedrich Seitz, Andrey Tarasov, Sergey V. Levchenko, Robert Schloegl, and Elias Frei

J. Am. Chem. Soc., **Just Accepted Manuscript** • Publication Date (Web): 14 Jan 2019

Downloaded from <http://pubs.acs.org> on January 14, 2019

Just Accepted

"Just Accepted" manuscripts have been peer-reviewed and accepted for publication. They are posted online prior to technical editing, formatting for publication and author proofing. The American Chemical Society provides "Just Accepted" as a service to the research community to expedite the dissemination of scientific material as soon as possible after acceptance. "Just Accepted" manuscripts appear in full in PDF format accompanied by an HTML abstract. "Just Accepted" manuscripts have been fully peer reviewed, but should not be considered the official version of record. They are citable by the Digital Object Identifier (DOI®). "Just Accepted" is an optional service offered to authors. Therefore, the "Just Accepted" Web site may not include all articles that will be published in the journal. After a manuscript is technically edited and formatted, it will be removed from the "Just Accepted" Web site and published as an ASAP article. Note that technical editing may introduce minor changes to the manuscript text and/or graphics which could affect content, and all legal disclaimers and ethical guidelines that apply to the journal pertain. ACS cannot be held responsible for errors or consequences arising from the use of information contained in these "Just Accepted" manuscripts.

Ni single atom catalysts for CO₂ activation

Marie-Mathilde Millet^[a], Gerardo Algara-Siller^[a], Sabine Wrabetz^[a], Aliaksei Mazheika^[b],

Frank Girgsdies^[a], Detre Teschner^[a,c], Friedrich Seitz^[a], Andrey Tarasov^[a], Sergey V.

Levchenko^[b,d,e], Robert Schlögl^[a,c], and Elias Frei^{*[a]}

[a] M.-M. Millet, Dr.G. Algara-Siller, Dr.S. Wrabetz, Dr.F. Girgsdies, Dr.D.Teschner, Dr.F.Seitz,

Dr.A. Tarasov, Prof.Dr.R. Schlögl, Dr.E. Frei

Department of Inorganic Chemistry

Fritz-Haber-Institut der Max-Planck-Gesellschaft

Faradayweg 4-6, 14195 Berlin (Germany)

[b] Dr. Aliaksei Mazheika, Dr. Sergey V. Levchenko

Department of Theory

Fritz-Haber-Institut der Max-Planck-Gesellschaft

Faradayweg 4-6, 14195 Berlin (Germany)

[c] Dr. Detre Teschner, Prof. Dr. R. Schlögl

Max-Planck-Institut für Chemische Energiekonversion

Abteilung Heterogene Reaktionen

Stiftstr. 34-36, 45470 Mülheim an der Ruhr (Germany)

[d] Dr. Sergey V. Levchenko

Center for Electrochemical Energy Storage

Skolkovo Institute of Science and Technology

Nobel Str. 3, 143026 Moscow (Russia)

[e] Dr. Sergey V. Levchenko

Materials Modeling and Development Laboratory

National University of Science and Technology „MISIS“

Leninskii av. 4, 119049 Moscow (Russia)

* E-mail: efrei@fhi-berlin.mpg.de

Keywords: Single atom Catalyst / Ni-Mg solid solution / CO₂ activation / Ni_xMg_{1-x}O / Reverse water-gas shift / Heterogeneous catalysis

1 Abstract

We report on the activation of CO₂ on Ni single atom catalysts. These catalysts were synthesized using a solid solution approach, by controlled substitution of 1-10 atom-% of Mg²⁺ by Ni²⁺ inside the MgO structure. The Ni atoms are preferentially located on the surface of the MgO, and as predicted by hybrid-functional calculations, prefer low-coordinated sites. The isolated Ni atoms are active for CO₂ conversion through the reverse water-gas shift (rWGS), but are unable to conduct its further hydrogenation to CH₄ (or MeOH), for which Ni clusters are needed. The CO formation rates correlate linearly with the concentration of Ni on the surface evidenced by XPS and microcalorimetry. The calculations show that the substitution of Mg atoms by Ni atoms on the surface of the oxide structure reduces the strength of the CO₂ binding at low-coordinated sites and also promotes H₂ dissociation. Astonishingly, the single atom catalysts stayed stable over 100 hours time on stream, after which no clusters or particle formation could be detected. Upon catalysis, a surface carbonate adsorbate-layer was formed, of which the decompositions appears to be directly linked to the aggregation of Ni. This study on atomically dispersed Ni species brings new fundamental understanding of Ni active sites for reactions involving CO₂, and clearly evidences the limits of single atom catalysis for complex reactions.

2 Introduction

Noble-metals stabilized on metal oxides are one of the most widely used heterogeneous catalysts also applied in the industry¹. The size of the metal particles is a cornerstone for the performances of such supported catalysts in terms of metal atom efficiency and selectivity, which both tend to decrease with increasing particle size and broadening size distributions². Hence there is a need for sophisticated preparation techniques to control with precision the size of those supported metal clusters. Furthermore, the diversity and irregularity of the clusters in size and shape strongly hinder the complete identification of the active site and as such, the understanding of the reaction. Reducing the complexity of such systems can be achieved by the largest conceivable reduction of both, the size and the size distribution of the metal particles, by the preparation of “single atom catalysts” (SAC). The first practical synthesis of single atom catalysts was performed by Zhang’s group^{2e}, achieving the preparation of isolated Pt atoms on an FeOx support. While the denomination of SAC is relatively recent^{2e}, the concept of “isolated active site within a solid catalyst” was introduced much earlier according to John Meurig Thomas³, and became prominent thanks to the early work of Grasselli *et al.*⁴. During the last years many studies were conducted on single atom catalysts, dealing with supported noble metals like Pt^{2e, 5}, Au^{2d, 5a, 6}, Ir⁷, Pd⁸, but rarely using cheaper and more earth-abundant transition metals.

The understanding of CO₂ activation reactions has become a topic undergoing intense study because of environmental considerations. Among the transition metals efficient for CO₂ activation and hydrogenation reactions, supported Ni catalysts are prominently represented⁹. These catalysts have been extensively studied in methanation¹⁰ and dry reforming of methane¹¹ reactions. The size of the Ni particles in such systems is known to have a large influence on the selectivity of the methanation reaction¹². Larger particles lead to more CH₄ selective catalysts, while small particles are more selective towards CO¹³. Recently, Vogt *et al.* provided some new mechanistic insights on the CO₂ methanation reaction by correlating the size of the Ni clusters (1-7nm), to the stability of the reaction intermediates¹⁴. Interestingly, they observed even for the smallest Ni clusters (≈1nm) the formation

of methane. In this study, we go a step further by focusing our interest on the preparation of Ni single atom catalysts, in particular for the hydrogenation of CO₂ to CO or CH₄. To our knowledge, such challenge has not yet been met successfully and only few studies were reported about single Ni atom catalysts, focusing only on electrocatalytic applications or Ni clusters within a single site concept^{11c, 15}.

Wet chemistry based synthesis methods have been selected for this purpose since, unlike physical deposition synthesis methods like sputtering¹⁶, they allow the production of larger amounts of catalyst, suitable for their full characterization or even practical industrial applications. One main criterion for the successful synthesis of SAC is to strongly anchor the metal species on the support to avoid their aggregation¹. To overcome this problem, we used the ability of NiO and MgO to form a solid solution as strategy to prevent the Ni from agglomerating. Both metal oxides crystallize in a face centered cubic (fcc) structure with almost identical lattice parameters (MgO: 0.4213nm, NiO: 0.41769nm)¹⁷. Additionally, MgO is a very suitable support for CO₂ activation reactions, since its strong basicity enhances the CO₂ adsorption capacity¹⁸.

In this study, we report for the first time on successful synthesis of Ni SAC in the range of 1-10(at.-%) in the MgO lattice (Ni_xMg_{1-x}O). The structure and composition of the precursors and catalysts were thoroughly analyzed with XRD, XPS, XRF, FTIR, STA-MS, microcalorimetry and electron microscopy. The activity in the rWGS reaction was measured and correlated to the catalyst properties. Additionally, DFT hybrid-functional calculations were performed to better elucidate the role of the Ni atoms with respect to catalytic performance and structural stability. The nature and properties of the active site will be discussed also in the context of Ni cluster formation as bridge to the Ni particle based high performance catalysts. Finally, this study addresses the highly important question related to the use of single atom catalyst as models for supported nanoparticle catalysts, and to their ability to conduct multi-electron redox reactions without limitations.

3 Methods

3.1 Catalysts preparation

Materials. $\text{Mg}(\text{NO}_3)_2 \cdot 6\text{H}_2\text{O}$ (99+%, Acros Organics), $\text{Ni}(\text{NO}_3)_2 \cdot 6\text{H}_2\text{O}$ (99+%, Acros Organics), Ammonia 25% (VWR Chemicals, NORMAPUR) and deionized water obtained from laboratory purification system.

Synthesis. The $\text{Ni}_x\text{Mg}_{1-x}(\text{OH})_2$ precursors were synthesized by co-precipitation from a Ni and Mg nitrate solution (Σ 1M) and a 1M Ammonia solution as precipitating agent, in an automated lab reactor. The equimolar mixture was chosen (as opposed to the stoichiometric one) to avoid the formation of $\text{Mg}_2\text{Ni}(\text{NH}_3)_6$. While stirring at 300 r.min^{-1} , both solutions were dosed at a rate of 10 g.min^{-1} , into deionized water (300ml) at a controlled temperature of 60°C . The resulting solution was aged for 1hour before cooling down to room temperature. The pH electrode was calibrated at 25°C with the buffer solutions pH=7 and pH=10 (Carl Roth ± 0.02). The pH increased strongly with the first drops of ammonia (pH=9.3), but then remained constant throughout the whole synthesis and ageing processes (around pH=8.8). All parameters of the synthesis were recorded and are shown in supporting information (Figure S1). The slurry was filtrated and the precipitate washed with deionized water until the conductivity was below 0.5 mS.cm^{-1} . The light green solid was dried at 80°C for 15 h with a heating ramp of 2°C.min^{-1} and then calcined in a rotating furnace at 600°C for 3h in a flow of 100 ml.min^{-1} consisting of 21% O_2 in Argon, with a heating ramp of 2°C.min^{-1} .

3.2 Characterization

XRD. The X-ray diffraction (XRD) measurements were performed in Bragg-Brentano geometry on a Bruker AXS D8 Advance II theta/theta diffractometer, using Ni filtered $\text{Cu K}\alpha$ radiation and a position sensitive energy dispersive LynxEye silicon strip detector. The sample powder was filled into the recess of a cup-shaped sample holder, the surface of the powder bed being flush with the sample holder edge (front loading). The powder XRD data were analyzed, and the lattice parameters calculated using a full pattern fitting, according to the Rietveld method as implemented in the TOPAS software [TOPAS version 5, copyright 1999-2014 Bruker AXS].

STA-MS. Simultaneous thermo analysis (TG/DSC) was performed on a Netzsch STA449 Jupiter thermoanalyzer, using 10-15mg of sample placed into an alumina crucible (85μl) without lid. Evolution of the gas phase during reaction was monitored with a quadrupole mass spectrometer (Pfeiffer, QMS200 Omnistar). The thermal decomposition was performed from room temperature to 1000°C, with a heating ramp of 2°C.min⁻¹ in a 21%O₂ in Ar atmosphere (100ml.min⁻¹). Experimental mass loss were calculated from 100 to 1000°C to avoid taking into account the adsorbed surface species (ex: water).

The specific CO₂ area was calculated using the following formula:

$$S_{\text{CO}_2} = n_s * S * N_A * \text{CSA}_{(\text{CO}_2 \text{ on MgO})} \quad (1)$$

Where n_s is the amount of CO₂ molecules, S the stoichiometric factor, N_A the Avogadro number ($6.022140857 \times 10^{23}$) and CSA the cross sectional area of a CO₂ molecule adsorbed on MgO ($22.1 \times 10^{-20} \text{ m}^2$)¹⁹.

Catalytic testing. The catalytic measurements were performed in a fixed bed flow reactor. 100mg of the oxidic compound (100-250 μm particle diameter) were loaded into a 6 mm inner diameter stainless steel reactor tube. It was first heated in argon to 350°C (1°C.min⁻¹, hold 1h) to get rid of volatile adsorbed species and then exposed at 200°C to 100ml.min⁻¹ of a Sabatier gas mixture (72 % H₂, 18% CO₂, 10% Ar for balance) at 30 bar pressure. Gas analysis was performed online by a gas chromatograph (Agilent 7890A) equipped with two channels, a thermal conductivity detector was used to analyze CO₂, CO and Argon, while a flame ionization detector was used to analyze MeOH and CH₄ (both of which were combined with different capillary columns: molesieve and plot-Q). All catalytic testings were performed under differential conditions (< 3% conversion). Testing with pure silica, at the same conditions revealed negligible formation rates, in the same order of magnitude than the one of the sample that did not contained any Nickel (pure MgO).

Microcalorimetry. Microcalorimetric experiments were carried out in a Calvet calorimeter (SETARAM MS70) combined with custom-designed high vacuum and gas dosing apparatus, which enables the

dosage of probe molecules within a range of 0.02 mmol and to calculate the amount of adsorbed molecules. The samples were degassed under UHV at 500 °C for 1 h with a heating ramp of 5 °C.min⁻¹. The pretreatment was conducted in a separate chamber connected to the calorimetric cell. The final pressure in the degassed cell was approximately 10⁻⁷ mbar. The cell was cooled to room temperature, placed inside the calorimeter, and connected to the microcalorimetric gas-adsorption system. Subsequently, CO₂ was dosed stepwise at 30°C. Pressure, adsorption temperature, and the heat signals were recorded during all dosing steps.

XPS. All samples were investigated as pressed pellets. XPS spectra were recorded using non-monochromatized Al K α (1486 eV) excitation and a hemispherical analyzer (Phoibos 150, SPECS). The binding energy (BE) scale was calibrated using standard Au 4f (7/2) and Cu 2p (3/2) procedure. Charging, in the range of 6-7 eV, was observed with the samples. Binding energy correction for charging was carried out by adjusting the Mg2p level to 50.3 eV. To calculate the elemental composition, the theoretical cross sections from Yeh and Lindau²⁰ were used.

TEM. Samples were characterized using a transmission electron microscope JEOL ARM 200F operated at 200 kV. Images were taken with scanning TEM (STEM) and high resolution TEM (HRTEM) modes.

XRF. X-ray fluorescence spectroscopy (XRF) was performed in a Bruker S4 Pioneer X-ray spectrometer. Sample preparation by melted pellets (100 mg sample with 8.9g of Li₂B₄O₇).

TPR. Temperature programmed reductions were performed in a fixed bed reactor, in a 5% H₂ in Argon gas mixture, with an heating rate of 5°C.min⁻¹ (100ml.min⁻¹ for 100mg catalyst). The H₂ consumption was monitored by a TCD detector. Prior to reduction, the catalysts were heated in Argon to 500°C (5°C.min⁻¹ for 1h) to get rid of adsorbed surface species. The Ni_{10%} sample “after catalysis” was taken out of the reactor and set in contact with air before reduction.

BET. Specific surface areas were determined by N₂ physisorption using the BET method²¹ in a Quantachrome Autosorb-1 machine. The samples were previously outgassed for 3.5 h at 80 °C.

In situ IR. The Ni_{10%} sample was pressed into a self supporting disc (40.2mg) and placed in the sample holder in the center of the furnace of the IR cell. The design of the IR cell was discussed

elsewhere²². After an activation in Argon at 500°C, the reactive gas was introduced in the cell at a flow rate of 120.6 ml.min⁻¹ and 10 bar pressure to reproduce the reaction conditions of the plug flow catalytic testing. The spectra were recorded with a Varian-670 FTIR spectrometer, with a resolution of 2 cm⁻¹ and an averaging of 128 scans to achieve satisfactory signal-to-noise ratio. The measurement was performed at 200, 250 and 300°C, after 8h of time on stream.

CO-adsorption IR. The low temperature IR measurements were carried out in transmission mode using a Perkin-Elmer 100 FTIR spectrometer equipped with a pre-treatment cell, enabling thermal treatments in controlled atmosphere. Background spectra were obtained by measuring a spectrum of the empty cell at -196°C. The Ni₁₀ self-supporting wafers were pre-treated once in vacuum to 500°C and once in an 72% H₂ atmosphere to 300°C (both with a heating rate of 5°C.min⁻¹, and hold at target temperature for 1h). The IR cell was then evacuated and cooled down to -196°C, for the progressive adsorption of CO (p_{CO}=0-5mbar).

3.3 Computational details

All calculations have been performed using hybrid density functional HSE²³ with $\omega = 0.11$ and fraction of exact exchange $\alpha = 0.3$, denoted – HSE(0.3). The validation of this method is shown in our previous work²⁴. We have used the FHI-aims code²⁵ which is all-electron with numerical atomic orbitals. The 'tight'²⁵ numerical settings and basis sets were employed. Relativistic effects were treated within zero-order regular approximation (ZORA)²⁶. Interatomic interaction at middle and large distances was improved using many-body dispersion correction (MBD)²⁷. The lattice parameter of cubic MgO was 4.217 Å, as obtained from the bulk calculations with HSE(0.3).

The calculations of adsorption were done using slab-periodic model. The k-grids for slabs were set with respect to 8x8x8 grid of cubic 8-atomic bulk unit cell. The slab thickness and cell sizes depended on the surface and considered adsorption sites. We used 5-layer slab with (2x2) unit cell for calculations of adsorption on (001) terrace. For simulations of (001) steps the 4-layer (2x3) slab with additional 4-atomic wide semilayer on top was used. The corner position was simulated with 3-layer (3x3) slab with 16-atomic square island on top. The (110) surface had 8-layers and the unit cell

1 depended on the coverage and desired Ni surface concentration. The vacuum-gap between slabs was
2
3
4
5
6
7
8
9
10
11
12
13
14
15
16
17
18
19
20
21
22
23
24
25
26
27
28
29
30
31
32
33
34
35
36
37
38
39
40
41
42
43
44
45
46
47
48
49
50
51
52
53
54
55
56
57
58
59
60

1 depended on the coverage and desired Ni surface concentration. The vacuum-gap between slabs was
2 about 200 Å. The adsorption of molecules was considered only on one side of the slab, so the dipole
3 correction was used to prevent unphysical overpolarization. All atoms were allowed to relax with
4 BFGS algorithm during the search of a minimum on potential energy surface. The procedure was
5 performed until maximal atomic forces did not exceed 10^{-2} eV/Å.
6 Adsorption energies were calculated as the difference between total energy of adsorbed system and
7 the sum of total energies of clean surface and gas-phase molecule. We applied the counterpoise
8 method for correction of superposition error.

4 Results and discussion

ID	Ni% (nominal)	Ni% (XRF)	Ni% (XPS)	FHI database
MgO	0	0	0	#25453
Ni_1	1	0.95	1.96	#23134
Ni_3	3	3.01	5.66	#25477
Ni_5	5	5.01	9.18	#27537
Ni_10	10	11.2	15.25	#23659
Ni_15	15	18.7	24.5	#23769

Table 1. Chemical constitution of prepared catalysts

4.1 Structural analysis of phase pure precursors and catalysts

Following a co-precipitation recipe (details see experimental part), a series of $\text{Ni}_x\text{Mg}_{1-x}\text{O}$ samples with varying Ni concentration (0 to 15 at.-%) was synthesized. The samples are named after their Ni concentration i.e. a sample containing 15 at.-% Ni will be named as Ni_15(OH)₂ for the precursor and Ni_15 for the oxidic compound. The XRD patterns of the precursors are illustrated in Figure S2. Rietveld refinement confirmed the phase purity of all samples. Since Ni(OH)₂ and Mg(OH)₂ have the same crystal structure (brucite type) and close ionic radii, $\text{Ni}_x\text{Mg}_{1-x}(\text{OH})_2$ solid solutions are formed. The evolution of the lattice parameters *a* and *c* as a function of the Ni content is shown Figure S3 and Table S1. A linear correlation between both lattice parameters and the Ni-loading is observed, confirming the successful incorporation of Ni in the Mg(OH)₂ structure as reported in the literature²⁸.

All precursors were analyzed using thermogravimetry (TG), coupled with simultaneous mass spectrometry (MS). The results are presented in Figure S4. The pure Mg(OH)₂ sample shows one characteristic endothermic peak with an onset temperature of 275°C. With increasing Ni-content this characteristic endothermic peak is shifted to lower onset temperatures. The presence of a single event (as opposed to two distinct ones) further evidences the successful formation of a solid solution, instead of a physical mixture of Ni(OH)₂ and Mg(OH)₂^{28b}. The theoretical and experimental weight losses are summarized in Table S3, and less than 1% deviation is observed. The phase pure

character of the precursors is also a prerequisite for the successful solid solution synthesis in the final catalysts.

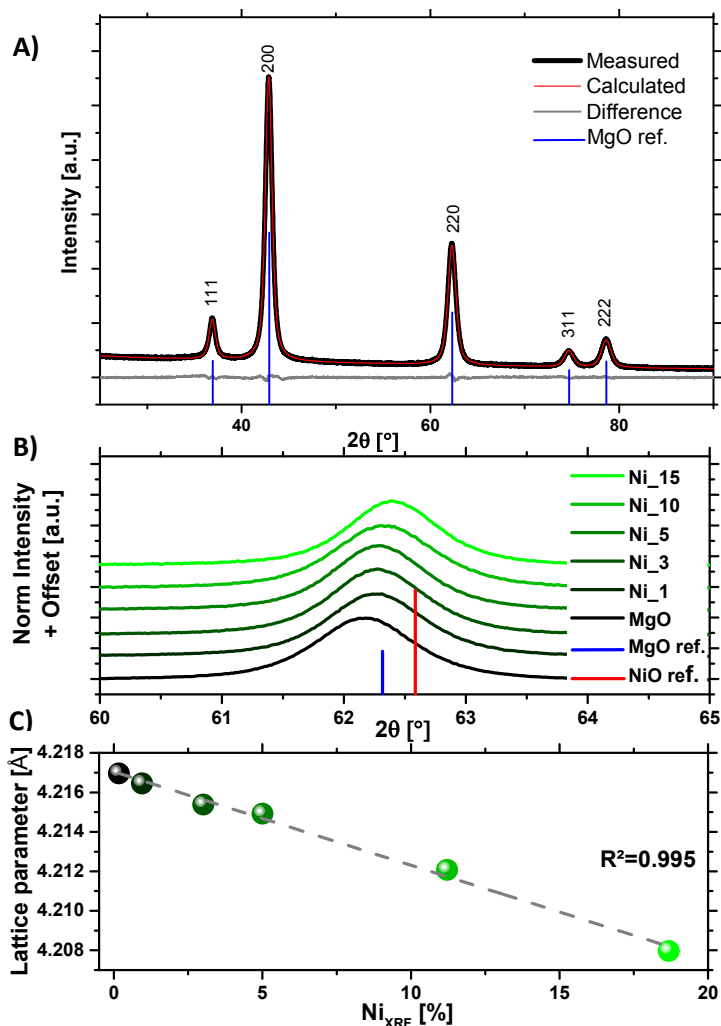


Figure 1. A) Rietveld fit of Ni₁₀ with the measured (black line) calculated (red line) diffraction patterns and the corresponding difference curve (grey line) B) Superposition of the 6 XRD patterns, zoom in the 60-65° region C) Variation of the lattice parameter *a* versus the Ni content determined by XRF

Figure 1A shows a full pattern Rietveld fit of the calcined Ni₁₀ sample (XRD patterns of all calcined samples are presented in Figure S5). The fit curve (red line) matches perfectly with the experiment (black line), also confirmed by the flat difference curve (blue line). Figure 1B shows a zoom of the 60-65° region of all diffractograms, exemplarily highlighting the shift of the 220 reflection to higher 2θ values with increasing Ni content. This corresponds to a continuous decrease of lattice parameter *a*

from 4.217 to 4.208 Å (Figure 1.C). Such behavior is characteristic of the successful incorporation of Ni inside the MgO structure^{17a} and a phase pure solid solution sample series. The error bars are invisible, as they are smaller than the size of the symbols used. All the lattice parameters and their estimated standard deviations are shown Table S2.

4.2 Dispersion

To further confirm the atomic distribution of the Ni atoms in the structure, scanning transmission electron microscopy (STEM) investigations were performed. The high-angle annular dark field (HAADF) STEM image in Figure 2 illustrates the isolated character of the Ni atoms (brighter spots) as part of the MgO lattice (Fig. 2B, magnification of 2A, STEM). This was also confirmed by the comparison of the dark- and bright-field image shown in Figure S6. Representative for all catalysts, the Ni₁₀ sample is shown, which has, due to its high Ni loading a high probability of cluster formation. After extensive analysis of different regions of all the samples, no Ni agglomerates were observed.

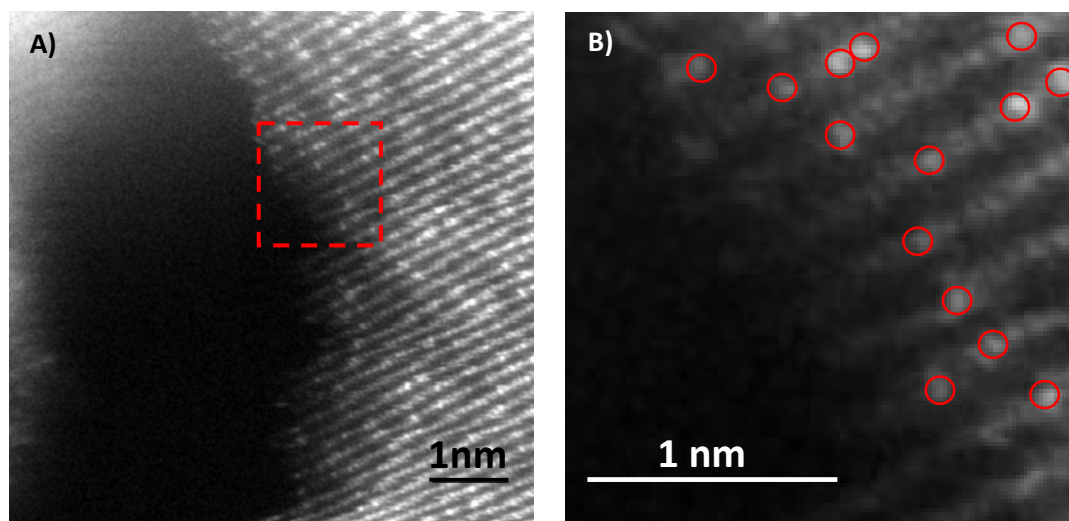


Figure 2. A) STEM-HAADF image of Ni₁₀ before catalytic testing B) Magnification of the selected area.

To guide the eye, some of the brighter spots were circled in red.

These findings are in line with the TPR profiles of the catalysts (Figure S7A). Since electron microscopy investigations are not representative of the entire sample, a more integral method was needed to confirm the dispersion of the Ni species inside the MgO structure. The absence of a low

temperature reduction event at about 350 °C, indicative for surface agglomerates, and only one strong signal at 750°C, indicative for Ni atoms embedded in the MgO structure²⁹, underlines the homogeneous character of the $\text{Ni}_x\text{Mg}_{1-x}\text{O}$ solid solution and the absence of NiO agglomerates at the surface.

4.3 Elemental composition

The global elemental composition (surface + bulk) was determined using X-ray fluorescence (XRF). The experimental values show a good agreement with the nominal ones (Table 1). According to a previous study, the most favorable position for a formal Mg^{2+} substitutions by Ni^{2+} ions, in a MgO structure is on its corners, coordinatively unsaturated²⁴. To investigate the Ni distribution in the structure, X-ray photoemission spectroscopy (XPS) was applied (Fig. 3A, Ni2p(3/2) core levels, Fig. S9 Mg2p spectra). The more surface sensitive XPS analysis reveals a strong surface enrichment by a factor of two for Ni in the solid solutions (Fig 3B, Table 1). The obtained spectra of Ni2p (870eV-850eV) show that only Ni^{2+} species are present over the whole range of concentration (Fig. 3A). Contrarily to the study of pure NiO, the presented Ni 2p XPS spectra did not show any peak splitting expected at 854-858eV. The main Ni 2p peak at 854eV in NiO, which is missing in our spectra, was identified in the literature as characteristic of Ni with neighboring Ni species³⁰. Its absence in this study is in line with the high dispersion of the Ni atoms in the MgO structure. A comparison of the surface composition vs. the global composition (Ni_{XPS} as a function of Ni_{XRF}), Figure 3B shows that from Ni_10, the surface composition is not evolving linearly. A surface saturation phenomenon is indicated for Ni_10 and Ni_15, resulting in a poorer surface Ni concentration (compared to their global Ni content) when compared to the samples with lower Ni loadings (Ni_1, Ni_3 and Ni_5).

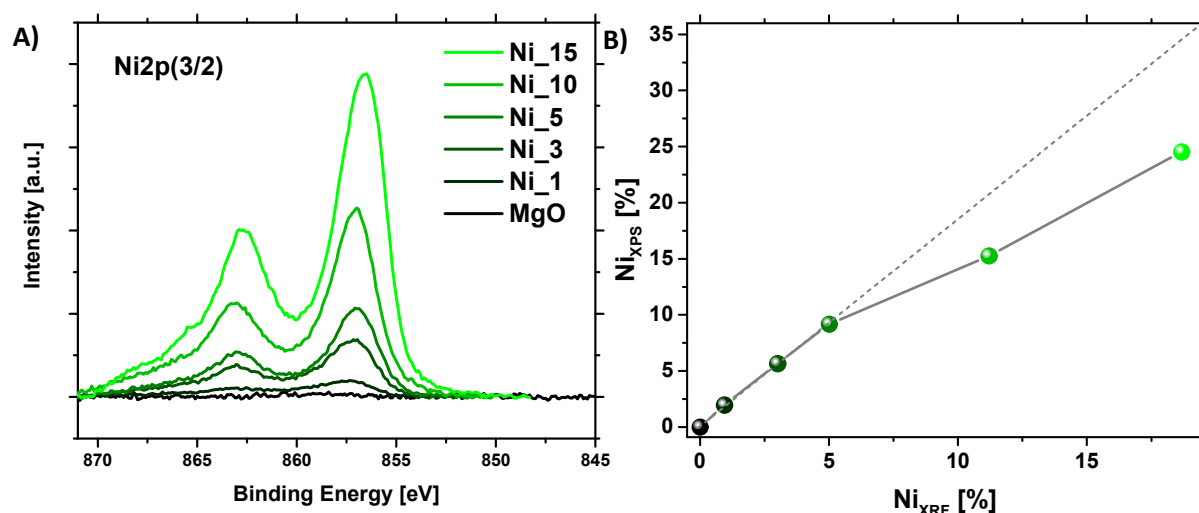


Figure 3. A) Ni_{2p} 3/2 spectra in the 870-845 eV region. B) Surface Ni concentration (measured by XPS) evolution versus the global Ni concentration (measured by XRF)

As XPS measurements also gain information from the sub-surface layers, another merely surface sensitive technique has to be applied. Microcalorimetry allows to chemically titrate the surface of the catalysts with CO₂ as probe molecule. The qualitative (differential heat of adsorption) and quantitative (amount of adsorbed molecules until saturation) information extracted from these measurements are shown in Figure S10. A linear correlation is obtained when comparing the amount of CO₂ adsorbed, measured by microcalorimetry, and the Ni concentration obtained by XPS (Fig. 5A). This strongly evidences that the Ni content gained by XPS correlates well with the Ni concentration on the surface of the catalysts. The linear dependency implies again a saturation effect for the Ni₁₀ sample (see also Figure S11A, amount of CO₂ titrated vs. XRF).

4.4 Catalytic testing

The catalysts were tested at 30 bar, between 200 and 300°C and in a gas mixture of H₂:CO₂ of 4:1 (for details see the experimental part). The H₂:CO₂ ratio, the low temperatures and the elevated pressure were chosen in order to favour the formation of CH₄ over CO, since this selectivity information serves as descriptor for multi-electron reactions. In order to study the reactivity of the isolated Ni atoms, the temperature of 300°C was not exceeded, as testing at higher temperatures (350°C) resulted in the formation of Ni-clusters of about 10 nm (Fig. 4B). Parallel to the Ni cluster formation, the reaction

rate of the by-product CH_4 increased as illustrated in Figure 4A. Details of the EDX mapping are presented Figure S12. Interestingly, at 350°C MeOH formation was recorded as a rather non-typical product of Ni catalysts. This might be explained by the intermediate character of the Ni cluster, more active than an atom but not yet a metallic particle with respect e.g. to its oxophilicity³¹ or the ability to activate H_2 . An ongoing formation of Ni clusters is suppressed as soon as we adjusted the temperature back to 300°C . Besides CH_4 as reaction product, a much higher reaction rate of CO is detected due to the already formed Ni clusters.

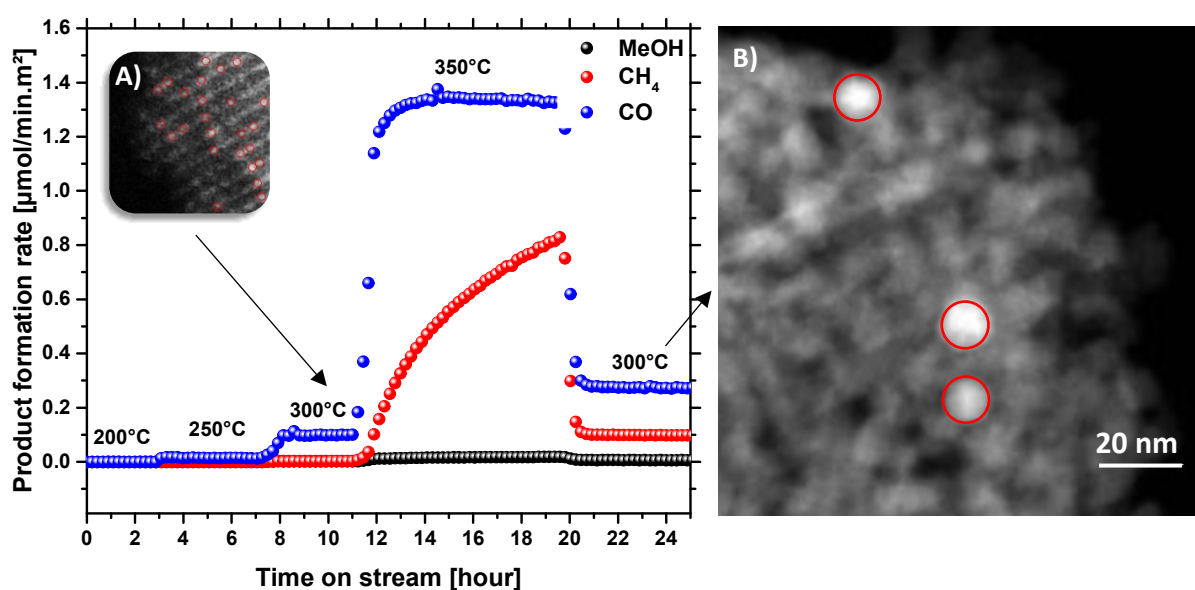


Figure 4. A) Product formation rate of Ni₁₀ at 30bar, different temperatures, upper corner left represent the sample after 300°C testing (Figure 7). B) TEM image of the sample after testing at 350°C .

The Ni₁₅ sample already showed CH_4 formation at 300°C and a large increase of the CO formation rate, similar to what is observed for the testing of Ni₁₀ at 350°C (Figure S13, Figure 4). As the cluster formation and the development of CH_4 as a by-product appear to be directly related, it is very likely that Ni clusters were already formed at the comparably low temperatures of 300°C in Ni₁₅ (sample with the highest Ni concentration). To ensure the reproducibility and to prove that no cluster formation occurred at 300°C , all samples were tested following an increasing and then decreasing temperature profile (Fig. S14). At 300°C , the catalysts were all 100% selective towards CO. During the testing period of 8h, no deactivation was observed. Figure 5B shows the CO formation rate (rWGS

1 reaction) as a function of the Ni content determined by XPS and as evidenced above (see also Fig. 5A)
2
3 the Ni concentration on the surface. Since the CO formation rate correlates linearly with the Ni
4
5 concentration on the surface, it is very likely that the Ni single atoms are directly involved in the
6
7 catalytic cycle. Due to the discrepancy with XRF results (saturation phenomenon, Fig. S11B) the Ni
8
9 atoms situated in the bulk do not significantly contribute to the observed reactivity. This
10
11 interpretation is in accordance with theory calculations, which show a negligible impact of Ni in sub-
12
13 surface region for CO₂ and H₂ adsorption (Table 2 and details in Table S8) when compared to Ni atoms
14
15 on the surface of the oxide. For example, according to theoretical calculations the adsorption
16
17 energies i.e. for CO₂ on terraces are between 62 and 68 kJ.mol⁻¹ for Ni free and Ni in the first or
18
19 second sub-surface layer of MgO (Fig. 6). The small but noticeable increase of CO₂ adsorption energy
20
21 in the case of MgO (001) surface with Ni in the second atomic layer is explained by additional
22
23 bonding of CO₃^{δ-} (including the surface oxygen) with Ni *d*-states. As the Ni is located deeper in
24
25 subsurface, the contribution of Ni states to the bonding is decreased.
26
27
28
29
30
31
32
33
34
35
36
37
38
39
40
41
42
43
44
45
46
47
48
49
50
51
52
53
54
55
56
57
58
59
60

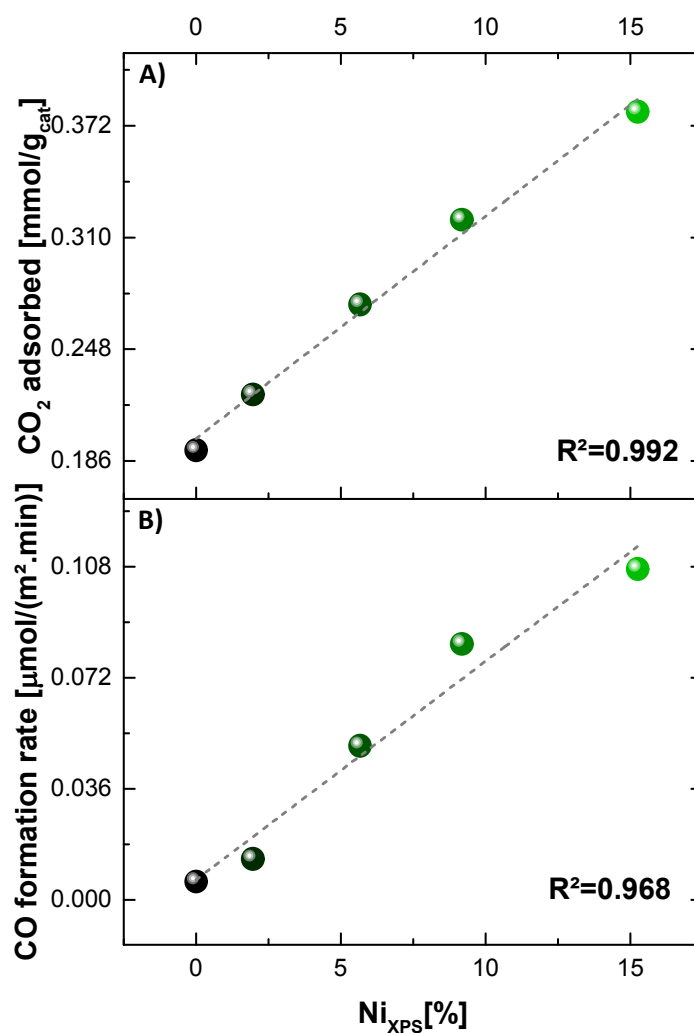


Figure 5. A) Evolution of the amount of CO_2 adsorbed (measured by microcalorimetry) versus the surface nickel concentration (measured by XPS) B) Evolution of the CO formation rate as a function of the surface nickel concentration (measured by XPS)

To gain further information about the stability of these catalysts, selected samples (Ni_3 and Ni_{10}) were tested over a period of 100 h TOS (Fig. S15A+B). Stable CO formation and the absence of CH_4 as a by-product was observed, which implies indirectly the absence of any cluster formation (as the cluster formation in our study was always accompanied by the development of CH_4 as by-product).

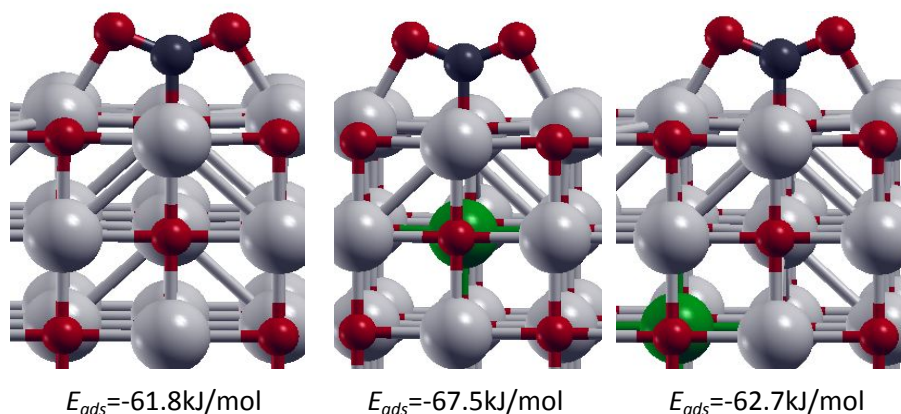


Figure 6. Example of the Influence of the adsorption site on the CO_2 adsorption energy for terrace sites. Green represents the Ni which substitutes one of the grey Mg atoms in the first and second sub-surface layer. Oxygen is shown in red and carbon in black.

4.5 Characterization after catalysis

After catalysis, the samples were thoroughly characterized (after 40 and 100 h TOS) with STEM, TPR, XRD and TG-MS. Figure 7A (and 7B as zoom-in) shows the STEM investigation of the Ni₁₀ catalyst after 40 h TOS. The analysis did not reveal the presence of any Ni particles or clusters as only single atoms of Ni in the MgO cubic structure were visible. The stable and selective catalytic performance is in agreement with the absence of Ni particles. To confirm this with a more integral method on a larger scale XRD Rietveld analysis was performed after catalysis (100h TOS, Ni₁₀). Figure 7C shows the absence of any new phases (hydroxides or carbonates) showing the absence of bulk transformation processes upon catalysis, again in line with the high stability of the catalysts even at elevated TOS. Furthermore, the lattice parameter a and the size of the coherent crystalline domains remained unchanged upon catalysis even after 100h TOS (variations smaller than 3e.s.d.: $a_{\text{before}} = 4.21126(7)$ vs. $a_{\text{after}} = 4.21104(7)$; $L_{\text{Vol}} \cdot \text{IB}_{\text{before}} = 9.42(12)$ vs. $L_{\text{Vol}} \cdot \text{IB}_{\text{after}} = 9.10(14)$).

TPR investigations after catalysis (40h TOS, Ni₁₀), revealed a specific reduction event at 350°C, which however could not be attributed to the reduction of NiO aggregates²⁹, as illustrated in Figure S7+S8, but to CO and CH₄ formation by hydrogenation of surface species. This confirms again that the testing at 300°C for extended TOS did not lead to the formation of Ni particles. Furthermore, this

1 experiment reveals that carbonate-based species on the surface of the catalysts are present after
2 reaction.

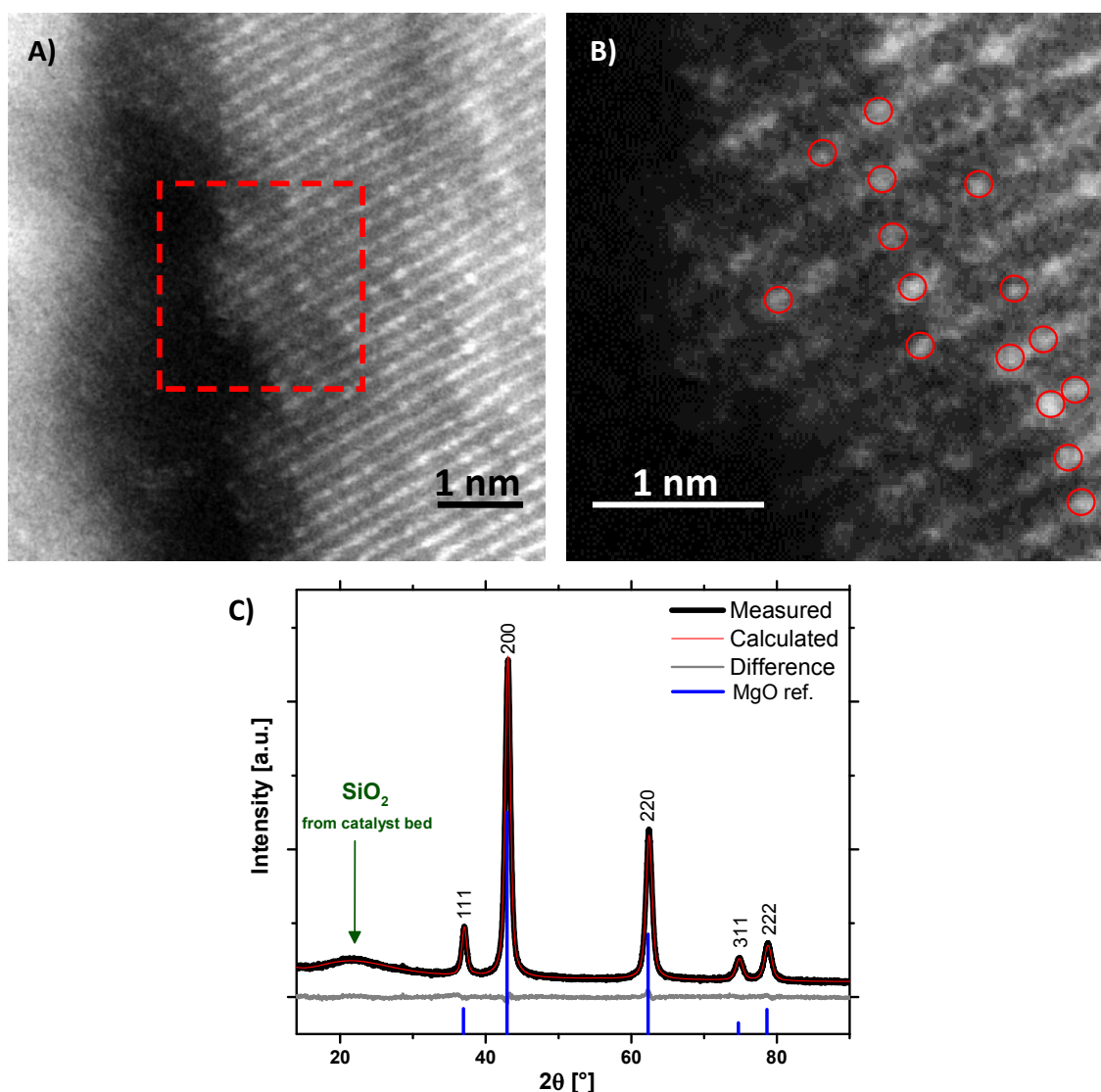


Figure 7. A) STEM-HAADF image of Ni₁₀ after catalysis B) STEM-HAADF image zoom of the indicated area. To guide the eye, some of the brighter spots were circled in red. C) Rietveld fit of Ni₁₀ after 100h time on stream without deactivation, with the measured (black line) calculated (red line) diffraction patterns and the corresponding difference curve (blue line)

TG-MS analysis before and after catalysis, revealed a clear surface modification upon testing. The thermal decomposition experiments showed a large release of CO₂ at 300°C, that was not observed on the fresh catalyst, together with an additional water release, indicating that the in-situ surface modification corresponds likely to the formation of hydrogenated-carbonate species (Figure S16).

1
2
3 1 Considering the amount of CO₂ released (measured by integration of the Mass Spectrometry signal
4
5 2 recorded upon thermal decomposition) and a homogeneous distribution of the adsorbates on the
6
7 3 available BET surface area, a coverage of approximately one monolayer is calculated (Table S4). As
8
9 4 expected, XRD was unable to resolve amorphous surface modifications including surface carbonates.

10
11
12 5 This over-layer formation appear to be closely linked with the stability of the SAC. While testing at
13
14 6 30bar leads to the stable formation of CO (Fig 5.A and S14), the testing at 1 bar leads to the
15
16 7 formation of CH₄ which suggests the formation of Ni clusters and particles at already 300°C, as shown
17
18 8 in Figure S17A and B. We observe that with ongoing TOS the selectivity towards CH₄ and the reaction
19
20 9 rates increase, in line with the catalyst behavior at 30 bar and 350°C (Fig. 4, Fig S17B).However,
21
22 10 testing at 1 bar after testing at 30 bar leads to stable production of CO with 100% selectivity. The
23
24 11 absence of CH₄ as a by-product consequently evidences the stability of the catalyst without the
25
26 12 formation of any Ni clusters (Figure S18). A reconstruction of the catalysts surface has thus taken
27
28 13 place in-situ at 30 bars. The stability of this surface modification (≤ 1 ML as shown Table S4), formed at
29
30 14 elevated pressures, seems to be directly related to the stability of the Ni atoms, as the agglomeration
31
32 15 of Ni is observed in its absence.

33
34
35
36
37
38 16 This is in good agreement with the results of the in-situ IR analysis shown Figure 8 A-C (see Table S5
39
40 17 the assignment of the IR modes). At the surface of the catalysts, were observed a mixture of different
41
42 18 carbonates and hydrogenated carbonates species. With increasing temperature, a progressive
43
44 19 decrease of the carbonate signals (1435,1529cm⁻¹) from the decomposition of the surface over-layer
45
46 20 is observed. This process is accompanied by an increase of the bicarbonate signal (1250cm⁻¹),
47
48 21 formate signals (1342,1606cm⁻¹), and the appearance of CH₄ (Fig. 8A, 1305 cm⁻¹; Fig. 8B,3016cm⁻¹).
49
50 22 This findings evidence once again the concerted fashion of a CO₂ release due to a progressive
51
52 23 instability of the surface over-layer, the agglomeration of the Ni and the formation of CH₄,
53
54 24 respectively. Besides, a pronounced shift in the formate area from 1607 to 1596cm⁻¹ is observed, as
55
56 25 shown in more details Figure 8C. While values around 1600-1606cm⁻¹ were attributed to formates
57
58 26 species on MgO³², values around 1591cm⁻¹ were recently reported for stretching vibration from
59
60

formates species on Ni⁰ nanoclusters¹⁴, further supporting the correlation of cluster formation and CH₄ production. The same shift was observed in the formate C-H area ($\approx 2900\text{cm}^{-1}$) as seen Figure S19. The stepwise red-shift of the formate stretching vibration with the formation of Ni clusters might be interpreted as a weakening of the conjugated C-O/C=O system on Ni clusters or at the metal/metal oxide interface, consequently visible in its increased catalytic performance (increasing CH₄ rates).

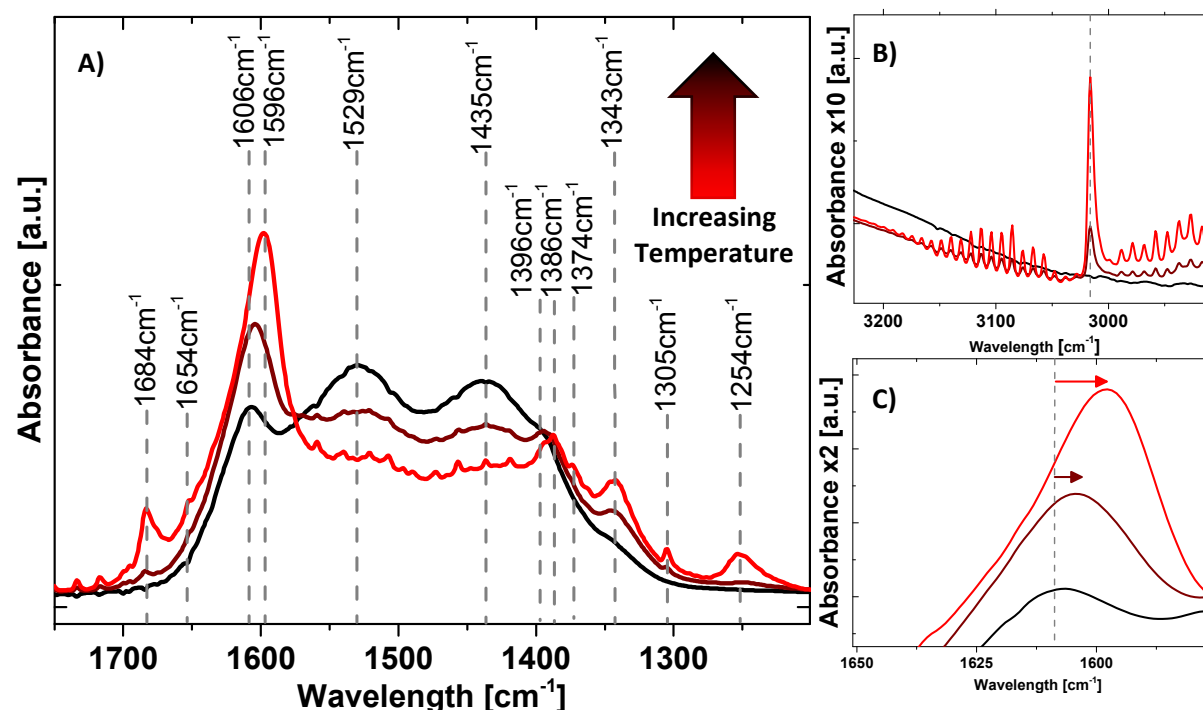


Figure 8. IR spectroscopy under reaction conditions, stepwise increase from 200 °C (black), to 250 °C (dark-red) to 300 °C (red). A) zoom in the 1200-1700 cm^{-1} area. B) zoom on the 2900-3200 cm^{-1} area C) zoom on the 1550-1650 cm^{-1} area

4.6 Final discussion

Microcalorimetry. Theoretical calculations (Table 2) predict for the adsorption of CO₂ three main types of sites: low energy sites [terraces -61.8 $\text{kJ}\cdot\text{mol}^{-1}$], intermediate energy sites [corners -160.2/-199.7 $\text{kJ}\cdot\text{mol}^{-1}$] and high energy sites [steps -219.0/-245.1 $\text{kJ}\cdot\text{mol}^{-1}$]. Comparing the qualitative analysis of the catalysts (Figure S10) in terms of their differential heats of adsorption, almost similar values are obtained (between 105 and 125 $\text{kJ}\cdot\text{mol}^{-1}$ for all samples). These energies could be attributed to the intermediary energy sites (corners), as under a mild vacuum pre-treatment, the high energy sites (steps) are not accessible (as seen by CO adsorption IR at 77K Figure S20 + Table S6).

Adsorption Energy (kJ/mol)						
Adsorption Site	CO ₂			H ₂ (dissociative adsorption)		
	Terraces	Corners	Steps	Terraces	Corners	Steps
NiMgO	-61.8	-160.2	-219.0	+109.0	-83.9	-98.4
MgO	-61.8	-199.7	-245.1	+171.7	-48.2	-51.1
MgO (Ni 1 st sublayer)	-67,5	-193.0	-236.4	+171.7	-47,3	-50.2
MgO (Ni 2 nd sublayer)	-62,7	-	-	-	-	-

Table 2. Calculation of the adsorption energy of CO₂, and of the dissociative adsorption of H₂ for different sites

The discrepancy observed between the theoretical values and the experimental ones could be explained, by the “uniform roughness” of the catalysts surface, the dependency of the E_{ads} on the CO₂ coverage³³ and by the Ni content (Table S7, S8) that tend to lower the adsorption energies.

The increase of the CO₂ uptake with the Ni concentration indicates that also the amount of available sites for titration (mainly corners) increased. This is in good agreement with the theoretical predictions suggesting that the most favorable position for a Ni²⁺ substitution is at the low coordinated sites (corners and steps) of the MgO. Further, the incorporation of Ni inside the structure might cause morphological changes, increasing the amount of corners in the structure, in order to allow the Ni atoms to reach their thermodynamically most favored position. The roughened surface rich in corners/steps is directly evidenced by overview TEM images (Fig. S21), which is in agreement with the presence of Ni on unsaturated sites.

Catalysis. We observe a linear evolution of the reactivity with the Ni surface concentration, clearly indicating that the Ni surface sites are involved in the catalytic cycle, while their isolation, and the absence of agglomeration explains the linear character of the correlation. Under reaction conditions, a surface adsorbate layer was formed (carbonate-based species). The stability of this reactant induced restructuring is directly linked with the stability of the catalysts and their high selectivity towards CO. The involvement of the surface Ni atoms in the catalytic cycle could be related to the poorer stability of carbonate-based intermediates on Ni sites, in accordance with the calculated

adsorption energy of CO₂ on Ni vs Mg (Table2, S7,S8). Ni would promote the formation of “CO₂ vacancies” in this carbonate layer and enable the activation of H₂ molecules leading to their catalytic dissociation. Indeed, to conduct the rWGS reaction, it is crucial to adsorb and dissociate the H₂ molecules, a process which is much more favorable on Ni atoms as part of the MgO instead of pure MgO. That means Ni changes the surface termination and population of corners and steps of the entire catalysts since coordinatively unsaturated sites are thermodynamically favored.²⁴ Besides this structural impact, Ni has a direct influence on the reactants, increasing the activation of H₂ and decreasing the stability of activated CO₂ accessible for its catalytic conversion.

Particle formation. While the isolated Ni atoms were active for the activation of CO₂, their selectivity was restricted to CO, and the formation of Ni clusters (even of a few nm) was necessary to form higher value-added products such as CH₄¹⁴ or even MeOH. Indeed, the single atoms are only able to take part in the 2e⁻ redox cycle while, to perform the full hydrogenation of CO₂ (the 8e⁻ redox cycle), Ni clusters are crucial. Furthermore, the product formation rates increased by a factor of three at the same temperatures after particle formation occurred (Fig. 4).

5 Conclusions

Through the synthesis of phase pure precursors and catalysts, we prepared for the first time Ni single atom catalysts using wet chemistry. Ni concentrations of up to 10 atom-% were achieved and identified as upper limit for the function of single atom catalyst. The anchoring of the Ni and its stabilization was achieved by a solid solution approach. A Ni surface enrichment of the solid solutions is observed, by both physical and chemical analysis methods, in agreement with the prediction made from first principle calculations²⁴. This enrichment has somehow its restrictions, as samples containing 10 atom-% Ni or more show a saturation phenomenon. These Ni single atom catalysts are active for CO₂ activation in the reverse-water-gas-shift reaction. A stable performance over time, which evolved linearly with the amount of Ni on the surface, is observed. We exclude that the dominant effect of this reactivity is a bulk effect. Further, we show that the main contribution is originated from the amount of Ni atoms on the surface of the catalysts. During catalysis a carbonate-

based over-layer was formed and its decomposition appears to be coupled to the Ni agglomeration. Finally, isolated Ni atoms were not able to hydrogenate CO₂ to higher value added products such as CH₄ or MeOH, for which Ni clusters are necessary. The simplification of the size of active sites towards single atoms seems to have limitations, since the ability to catalyze a multi electron reaction is attributed to at least Ni clusters. The selectivity change towards CH₄ and the progressive increase of the reaction rates (CO and CH₄) for the samples with Ni clusters give insights into the different reactivity regimes occurring before and after the particle formation. The reactant induced surface over-layer mechanism for the Ni single atom catalysts is consecutively substituted by a formate based one, in which the continuously growing Ni cluster/particles decrease the formate stability. This leads to higher reaction rates and higher CH₄ selectivities. Within this Ni_xMg_{1-x}O solid solution study we bridge for the first time the Ni single atom to Ni cluster regime as example of the limited applicability of SAC as high performance catalysts. Besides, this fundamental contribution to the mechanistic understanding in the development of catalytic selectivity and activity serves as new approach adaptable to other reactions and systems forming solid solutions.

6 Supporting Information

Please find additional information on the synthesis protocol, details of all powder X-ray diffraction measurements, electron microscopy, microcalorimetry, details of the catalytic testing, details of the thermal analysis, IR-spectroscopy and the theoretical calculations in the SI.

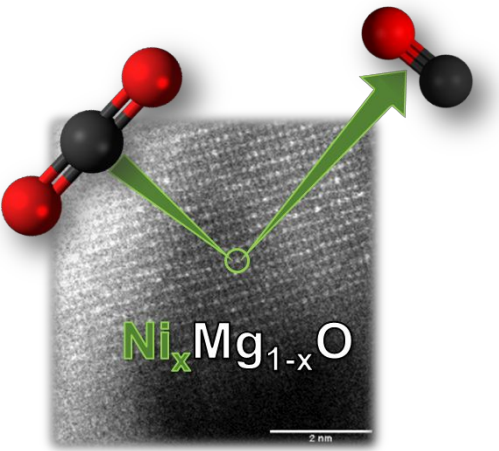
7 Acknowledgments

The authors thank J. Plagemann and M. Hashagen for BET analysis, Dr. O. Timpe for XRF analysis, and J. Allan for TGMS measurements. Marie-Mathilde Millet thanks Unicat for financial support, “FKZ: EXC 314/1 UNICAT”. Calculations of CO₂ and H₂ activation at surfaces were supported by the grant from the Ministry of Education and Science of the Russian Federation (Grant No. 14.Y26.31.0005). Analysis of the effects of doping on surface chemical properties was supported by the Ministry of Education and Science of the Russian Federation in the framework of Increase Competitiveness

1
2
3
4
5
6
7
8
9
10
11
12
13
14
15
16
17
18
19
20
21
22
23
24
25
26
27
28
29
30
31
32
33
34
35
36
37
38
39
40
41
42
43
44
45
46
47
48
49
50
51
52
53
54
55
56
57
58
59
60

1 Program of NUST "MISIS" (No. K2-2017-080) implemented by a governmental decree dated 16 March
2 2013, No.211.

6 **Graphical abstract**



References

1. Yang, X.-F.; Wang, A.; Qiao, B.; Li, J.; Liu, J.; Zhang, T., Single-Atom Catalysts: A New Frontier in Heterogeneous Catalysis. *Acc. Chem. Res.* **2013**, *46* (8), 1740-1748.
2. (a) Herzing, A. A.; Kiely, C. J.; Carley, A. F.; Landon, P.; Hutchings, G. J., Identification of Active Gold Nanoclusters on Iron Oxide Supports for CO Oxidation. *Science* **2008**, *321* (5894), 1331-1335; (b) Turner, M.; Golovko, V. B.; Vaughan, O. P. H.; Abdulkhin, P.; Berenguer-Murcia, A.; Tikhov, M. S.; Johnson, B. F. G.; Lambert, R. M., Selective oxidation with dioxygen by gold nanoparticle catalysts derived from 55-atom clusters. *Nature* **2008**, *454* (7207), 981-983; (c) Molina, L. M.; Lee, S.; Sell, K.; Barcaro, G.; Fortunelli, A.; Lee, B.; Seifert, S.; Winans, R. E.; Elam, J. W.; Pellin, M. J.; Barke, I.; von Oeynhausen, V.; Lei, Y.; Meyer, R. J.; Alonso, J. A.; Fraile Rodríguez, A.; Kleibert, A.; Giorgio, S.; Henry, C. R.; Meiwe-Broer, K.-H.; Vajda, S., Size-dependent selectivity and activity of silver nanoclusters in the partial oxidation of propylene to propylene oxide and acrolein: A joint experimental and theoretical study. *Catalysis Today* **2011**, *160* (1), 116-130; (d) Zhang, X.; Shi, H.; Xu, B.-Q., Catalysis by Gold: Isolated Surface Au³⁺ Ions are Active Sites for Selective Hydrogenation of 1,3-Butadiene over Au/ZrO₂ Catalysts. *Angewandte Chemie International Edition* **2005**, *44* (43), 7132-7135; (e) Qiao, B.; Wang, A.; Yang, X.; Allard, L. F.; Jiang, Z.; Cui, Y.; Liu, J.; Li, J.; Zhang, T., Single-atom catalysis of CO oxidation using Pt₁/FeO_x. *Nat. Chem.* **2011**, *3* (8), 634-641; (f) Murzin, D. Y., On Cluster Size Dependent Activity and Selectivity in Heterogeneous Catalysis. *Catal. Lett.* **2012**, *142* (11), 1279-1285; (g) Rioux, R. M.; Hsu, B. B.; Grass, M. E.; Song, H.; Somorjai, G. A., Influence of Particle Size on Reaction Selectivity in Cyclohexene Hydrogenation and Dehydrogenation over Silica-Supported Monodisperse Pt Particles. *Catal. Lett.* **2008**, *126* (1-2), 10; (h) Kuhn, J. N.; Huang, W.; Tsung, C.-K.; Zhang, Y.; Somorjai, G. A., Structure Sensitivity of Carbon-Nitrogen Ring Opening: Impact of Platinum Particle Size from below 1 to 5 nm upon Pyrrole Hydrogenation Product Selectivity over Monodisperse Platinum Nanoparticles Loaded onto Mesoporous Silica. *J. Am. Chem. Soc.* **2008**, *130* (43), 14026-14027.
3. Thomas, J. M., How Far is the Concept of Isolated Active Sites Valid in Solid Catalysts? *Top Catal.* **2008**, *50* (1-4), 98-105.
4. (a) Callahan, J. L.; Grasselli, R. K., A selectivity factor in vapor-phase hydrocarbon oxidation catalysis. *AIChE J.* **1963**, *9* (6), 755-760; (b) Grasselli, R. K.; Buttrey, D. J.; DeSanto Jr, P.; Burrington, J. D.; Lugmair, C. G.; Volpe Jr, A. F.; Weingand, T., Active centers in Mo-V-Nb-Te-Ox (amm)oxidation catalysts. *Catalysis Today* **2004**, *91-92*, 251-258; (c) Grasselli, R. K., Fundamental Principles of Selective Heterogeneous Oxidation Catalysis. *Top Catal.* **2002**, *21* (1-3), 79-88.
5. (a) Gu, X.-K.; Qiao, B.; Huang, C.-Q.; Ding, W.-C.; Sun, K.; Zhan, E.; Zhang, T.; Liu, J.; Li, W.-X., Supported Single Pt₁/Au₁ Atoms for Methanol Steam Reforming. *ACS Catal.* **2014**, *4* (11), 3886-3890; (b) Nie, L.; Mei, D.; Xiong, H.; Peng, B.; Ren, Z.; Hernandez, X. I. P.; DeLaRiva, A.; Wang, M.; Engelhard, M. H.; Kovarik, L.; Datye, A. K.; Wang, Y., Activation of surface lattice oxygen in single-atom Pt/CeO₂ for low-temperature CO oxidation. *Science* **2017**, *358* (6369), 1419-1423.
6. Qiao, B.; Liang, J.-X.; Wang, A.; Xu, C.-Q.; Li, J.; Zhang, T.; Liu, J. J., Ultrastable single-atom gold catalysts with strong covalent metal-support interaction (CMSI). *Nano Res.* **2015**, *8* (9), 2913-2924.
7. (a) Liang, J.-X.; Lin, J.; Yang, X.-F.; Wang, A.-Q.; Qiao, B.-T.; Liu, J.; Zhang, T.; Li, J., Theoretical and Experimental Investigations on Single-Atom Catalysis: Ir₁/FeO_x for CO Oxidation. *J. Phys. Chem. C* **2014**, *118* (38), 21945-21951; (b) Lin, J.; Wang, A.; Qiao, B.; Liu, X.; Yang, X.; Wang, X.; Liang, J.; Li, J.; Liu, J.; Zhang, T., Remarkable Performance of Ir₁/FeO_x Single-Atom Catalyst in Water Gas Shift Reaction. *J. Am. Chem. Soc.* **2013**, *135* (41), 15314-15317.
8. Aich, P.; Wei, H.; Basan, B.; Kropf, A. J.; Schweitzer, N. M.; Marshall, C. L.; Miller, J. T.; Meyer, R., Single-Atom Alloy Pd-Ag Catalyst for Selective Hydrogenation of Acrolein - The Journal of Physical Chemistry C (ACS Publications). **2015**, *119* (32), 18140.
9. (a) Silaghi, M.-C.; Comas-Vives, A.; Copéret, C., CO₂ Activation on Ni/γ-Al₂O₃ Catalysts by First-Principles Calculations: From Ideal Surfaces to Supported Nanoparticles. *ACS Catal.* **2016**, *6* (7), 4501-4505; (b) Lin, W.; Stocker, K. M.; Schatz, G. C., Mechanisms of Hydrogen-Assisted CO₂ Reduction on Nickel. *J. Am. Chem. Soc.* **2017**, *139* (13), 4663-4666; (c) Heine, C.; Lechner, B. A. J.;

- 1 Bluhm, H.; Salmeron, M., Recycling of CO₂: Probing the Chemical State of the Ni(111) Surface during
2 the Methanation Reaction with Ambient-Pressure X-Ray Photoelectron Spectroscopy. *J. Am. Chem.*
3 *Soc.* **2016**, *138* (40), 13246-13252; (d) Roiaz, M.; Monachino, E.; Dri, C.; Greiner, M.; Knop-Gericke, A.;
4 Schlögl, R.; Comelli, G.; Vesselli, E., Reverse Water–Gas Shift or Sabatier Methanation on Ni(110)?
5 Stable Surface Species at Near-Ambient Pressure. *J. Am. Chem. Soc.* **2016**, *138* (12), 4146-4154.
6 10. Garbarino, G.; Riani, P.; Magistri, L.; Busca, G., A study of the methanation of carbon dioxide
7 on Ni/Al₂O₃ catalysts at atmospheric pressure. *International Journal of Hydrogen Energy* **2014**, *39*
8 (22), 11557-11565.
9 11. (a) Mette, K.; Kühl, S.; Düdder, H.; Kähler, K.; Tarasov, A.; Muhler, M.; Behrens, M., Stable
10 Performance of Ni Catalysts in the Dry Reforming of Methane at High Temperatures for the Efficient
11 Conversion of CO₂ into Syngas. *ChemCatChem* **2014**, *6* (1), 100-104; (b) Tomishige, K., Syngas
12 production from methane reforming with CO₂/H₂O and O₂ over NiO–MgO solid solution catalyst in
13 fluidized bed reactors. *Catalysis Today* **2004**, *89* (4), 405-418; (c) Zuo, Z.; Liu, S.; Wang, Z.; Liu, C.;
14 Huang, W.; Huang, J.; Liu, P., Dry Reforming of Methane on Single-Site Ni/MgO Catalysts: Importance
15 of Site Confinement. *ACS Catal.* **2018**, *8* (10), 9821-9835.
16 12. Wu, H. C.; Chang, Y. C.; Wu, J. H.; Lin, J. H.; Lin, I. K.; Chen, C. S., Methanation of CO₂ and
17 reverse water gas shift reactions on Ni/SiO₂ catalysts: the influence of particle size on selectivity and
18 reaction pathway. **2015**, *5* (8), 4154-4163.
19 13. (a) Lu, B.; Kawamoto, K., Preparation of mesoporous CeO₂ and monodispersed NiO particles
20 in CeO₂, and enhanced selectivity of NiO/CeO₂ for reverse water gas shift reaction. *Materials*
21 *Research Bulletin* **2014**, *53*, 70-78; (b) Chen, C.-S.; Budi, C. S.; Wu, H.-C.; Saikia, D.; Kao, H.-M., Size-
22 Tunable Ni Nanoparticles Supported on Surface-Modified, Cage-Type Mesoporous Silica as Highly
23 Active Catalysts for CO₂ Hydrogenation. *ACS Catal.* **2017**, *7* (12), 8367-8381.
24 14. Vogt, C.; Groeneveld, E.; Kamsma, G.; Nachtegaal, M.; Lu, L.; Kiely, C. J.; Berben, P. H.; Meirer,
25 F.; Weckhuysen, B. M., Unravelling structure sensitivity in CO₂ hydrogenation over nickel. *Nature*
26 *Catalysis* **2018**, *1* (2), 127-134.
27 15. (a) Qiu, H. J.; Ito, Y.; Cong, W.; Tan, Y.; Liu, P.; Hirata, A.; Fujita, T.; Tang, Z.; Chen, M.,
28 Nanoporous Graphene with Single-Atom Nickel Dopants: An Efficient and Stable Catalyst for
29 Electrochemical Hydrogen Production. *Angewandte Chemie International Edition* **2015**, *54* (47),
30 14031-14035; (b) Zhao, C.; Dai, X.; Yao, T.; Chen, W.; Wang, X.; Wang, J.; Yang, J.; Wei, S.; Wu, Y.; Li,
31 Y., Ionic Exchange of Metal–Organic Frameworks to Access Single Nickel Sites for Efficient
32 Electroreduction of CO₂. *J. Am. Chem. Soc.* **2017**, *139* (24), 8078-8081; (c) Fei, H.; Dong, J.; Feng, Y.;
33 Allen, C. S.; Wan, C.; Voloskiy, B.; Li, M.; Zhao, Z.; Wang, Y.; Sun, H.; An, P.; Chen, W.; Guo, Z.; Lee, C.;
34 Chen, D.; Shakir, I.; Liu, M.; Hu, T.; Li, Y.; Kirkland, A. I.; Duan, X.; Huang, Y., General synthesis and
35 definitive structural identification of MN₄C₄ single-atom catalysts with tunable electrocatalytic
36 activities. *Nature Catalysis* **2018**, *1* (1), 63-72.
37 16. Gonçalves, R. V.; Vono, L. L. R.; Wojcieszak, R.; Dias, C. S. B.; Wender, H.; Teixeira-Neto, E.;
38 Rossi, L. M., Selective hydrogenation of CO₂ into CO on a highly dispersed nickel catalyst obtained by
39 magnetron sputtering deposition: A step towards liquid fuels. *Applied Catalysis B: Environmental*
40 **2017**, *209*, 240-246.
41 17. (a) Kuzmin, A.; Mironova, N., Composition dependence of the lattice parameter in NiMg_{1-x}CO
42 solid solutions. *Journal of physics. Condensed matter* **1998**, *10* (36), 7937-7944; (b) Kuzmin, A.;
43 Mironova, N.; Purans, J.; Rodionov, A., X-ray absorption spectroscopy study of NiMg_{1-x}CO solid
44 solutions on the Ni K edge. *J. Phys.: Condens. Matter* **1995**, *7* (48).
45 18. (a) Tomishige, K.; Yamazaki, O.; Chen, Y.; Yokoyama, K.; Li, X.; Fujimoto, K., Development of
46 ultra-stable Ni catalysts for CO₂ reforming of methane. *Catalysis Today* **1998**, *45* (1–4), 35-39; (b) Hu,
47 Y. H., Solid-solution catalysts for CO₂ reforming of methane. *Catalysis Today* **2009**, *148* (3–4), 206-
48 211; (c) Carreiro, J. A. S. P.; Baerns, M., Oxidative coupling of methane. *Journal of Catalysis* **1989**, *117*
49 (1), 258-265.
50 19. McClellan, A. L.; Harnsberger, H. F., Cross-sectional areas of molecules adsorbed on solid
51 surfaces. *Journal of Colloid and Interface Science* **1967**, *23* (4), 577-599.

20. Yeh, J. J.; Lindau, I., Atomic subshell photoionization cross sections and asymmetry parameters: $1 \leq Z \leq 103$. *Atomic Data and Nuclear Data Tables* **1985**, 32 (1), 1-155.
21. Brunauer, S.; Emmett, P. H.; Teller, E., Adsorption of Gases in Multimolecular Layers. *J. Am. Chem. Soc.* **1938**, 60, 309--319.
22. Farra, R.; Wrabetz, S.; Schuster, M. E.; Stotz, E.; Hamilton, N. G.; Amrute, A. P.; Pérez-Ramírez, J.; López, N.; Teschner, D., Understanding CeO₂ as a Deacon catalyst by probe molecule adsorption and in situ infrared characterisations. *Phys. Chem. Chem. Phys.* **2013**, 15 (10), 3454-3465.
23. Heyd, J.; Scuseria, G. E.; Ernzerhof, M., Hybrid functionals based on a screened Coulomb potential. *The Journal of Chemical Physics* **2003**, 118 (18), 8207-8215.
24. Mazheika, A.; Levchenko, S. V., Ni Substitutional Defects in Bulk and at the (001) Surface of MgO from First-Principles Calculations. *J. Phys. Chem. C* **2016**, 120 (47), 26934-26944.
25. Blum, V.; Gehrke, R.; Hanke, F.; Havu, P.; Havu, V.; Ren, X.; Reuter, K.; Scheffler, M., Ab initio molecular simulations with numeric atom-centered orbitals. *Computer Physics Communications* **2009**, 180 (11), 2175-2196.
26. Lenthe, E. v.; Baerends, E. J.; Snijders, J. G., Relativistic regular two-component Hamiltonians. *The Journal of Chemical Physics* **1993**, 99 (6), 4597-4610.
27. Tkatchenko, A.; DiStasio, R. A.; Car, R.; Scheffler, M., Accurate and Efficient Method for Many-Body van der Waals Interactions. *Phys. Rev. Lett.* **2012**, 108 (23), 236402.
28. (a) Asencios, Y. J. O.; Bellido, J. D. A.; Assaf, E. M., Synthesis of NiO–MgO–ZrO₂ catalysts and their performance in reforming of model biogas. *Applied Catalysis A: General* **2011**, 397 (1–2), 138-144; (b) Li, Y.; Lu, G.; Ma, J., Highly active and stable nano NiO–MgO catalyst encapsulated by silica with a core–shell structure for CO₂ methanation. *RSC Adv.* **2014**, 4 (34), 17420-17428.
29. (a) Arena, F.; Frusteri, F.; Parmaliana, A.; Giordano, N., On the reduction of NiO forms in magnesia supported catalysts. *React Kinet Catal Lett* **1990**, 42 (1), 121-126; (b) Jafarbegloo, M.; Tarlani, A.; Mesbah, A. W.; Muzart, J.; Sahebdehfar, S., NiO–MgO Solid Solution Prepared by Sol–Gel Method as Precursor for Ni/MgO Methane Dry Reforming Catalyst: Effect of Calcination Temperature on Catalytic Performance. *Catal Lett* **2016**, 146 (1), 238-248; (c) Parmaliana, A.; Arena, F.; Frusteri, F.; Giordano, N., Temperature-programmed reduction study of NiO–MgO interactions in magnesia-supported Ni catalysts and NiO–MgO physical mixture. *J. Chem. Soc., Faraday Trans.* **1990**, 86 (14), 2663-2669.
30. Alders, D.; Voogt, F. C.; Hibma, T.; Sawatzky, G. A., Nonlocal screening effects in 2p x-ray photoemission spectroscopy of NiO (100). *Phys. Rev. B* **1996**, 54 (11), 7716-7719.
31. Dietz, L.; Piccinin, S.; Maestri, M., Mechanistic Insights into CO₂ Activation via Reverse Water–Gas Shift on Metal Surfaces. *J. Phys. Chem. C* **2015**, 119 (9), 4959-4966.
32. (a) Busca, G.; Lamotte, J.; Lavalley, J. C.; Lorenzelli, V., FT-IR study of the adsorption and transformation of formaldehyde on oxide surfaces. *J. Am. Chem. Soc.* **1987**, 109 (17), 5197-5202; (b) Busca, G.; Lorenzelli, V., Infrared spectroscopic identification of species arising from reactive adsorption of carbon oxides on metal oxide surfaces. *Materials Chemistry* **1982**, 7 (1), 89-126; (c) Trillo, J. M.; Munuera, G.; Criado, J. M., Catalytic Decomposition of Formic Acid on Metal Oxides. *Catalysis Reviews* **1972**, 7 (1), 51-86.
33. Solis, B. H.; Cui, Y.; Weng, X.; Seifert, J.; Schauerhmann, S.; Sauer, J.; Shaikhutdinov, S.; Freund, H.-J., Initial stages of CO₂ adsorption on CaO: a combined experimental and computational study. *Phys. Chem. Chem. Phys.* **2017**, 19 (6), 4231-4242.